



Facile synthesis of highly active LaCoO₃/MgO composite perovskite via simultaneous co-precipitation in supercritical water

Jingyi Zhang^{a,b}, Xiaole Weng^{a,b,*}, Zhongbiao Wu^{a,b,*}, Yue Liu^{a,b}, Haiqiang Wang^{a,b}

^a Department of Environmental Engineering, Zhejiang University, Hangzhou 310027, PR China

^b Zhejiang Provincial Engineering Research Centre of Industrial Boiler & Furnace Flue Gas Pollution Control, Hangzhou 310027, PR China

ARTICLE INFO

Article history:

Received 20 April 2012

Received in revised form 17 July 2012

Accepted 20 July 2012

Available online 27 July 2012

Keywords:

Supercritical water

VOCs

Perovskite

Catalytic oxidation

Composite

ABSTRACT

In this paper, LaCoO₃/MgO composite perovskites were synthesized via a facile route using supercritical water and a more conventional citrate route. The resultant samples were denoted as sc-LCM and cr-LCM, respectively, which were subsequently subjected to a range of analytical techniques, including XRD, HAADF-STEM, HR-TEM, BET, H₂-TPR, O₂-TPD, etc. Experimental results showed that the sc-LCM sample had a well dispersed “support dispersion” feature (i.e. perovskites were dispersed on MgO supports), which yielded higher surface area and better oxygen desorption and reduction capability than the cr-LCM sample (with “among dispersion” feature, i.e. perovskites were dispersed among MgO particles), hence showing good performance in toluene and methane oxidation tests. We proposed that the “support dispersion” model in the sc-LCM sample could be more beneficial for the design of composite perovskites, which could not only ensure the functioning of MgO as sintering barriers but also provide sufficient contacting of LaCoO₃ particles with MgO support, leading to more oxygen deficiency in the structure as well as abundant weakly chemisorbed oxygen. We expect that the results present herein could give a new thought for the syntheses of composite perovskites with higher surface area and better catalytic activity.

© 2012 Elsevier B.V. All rights reserved.

1. Introduction

Today, development of advanced catalysts are beginning to attract tremendous attentions as the increasing demand for ever improvements in performance, functionality and more miniaturization at a reasonable cost. Synthetic techniques are the most important factor that closely linked to the properties of catalysts, particularly for composite catalysts, where the nature of resultant dispersion of any active species [1] and the interaction between the active species and supports [2], could effectively dominate their properties. Hence, synthetic routes that can offer homogenous dispersion and strong interaction of their products would be very much of interest in this regard.

Recently, perovskites have been extensively applied as catalysts in the applications such as selective catalytic reduction of NOx from automotive exhausts [3], carbon dioxide reforming of methane [4], catalytic oxidation of volatile organic compounds (VOCs) [5–8], photocatalytic degradation of azo dyes [9]. An usual ABO₃ perovskite has a super-structure with a ReO₃-type framework built up by incorporation of A cations into BO₆ octahedra [10]. The low cost, great diversity, high thermal stability and mechanical strength make the perovskites very promising materials for catalysis application. However, the catalytic performance of perovskites is still not satisfied, which is severely hindered by their particularly low surface area (generally several m² g⁻¹) and strong tendency to sinter during aging, limiting their practical applications. As such, numerous efforts have been devoted to increase the surface area of perovskites via either alternative synthesis routes (e.g. reactive grinding [11]) or structural modifications (e.g. forming composite perovskites [12–14]). Although the former (taking reactive grinding route for example) had indeed resulted in remarkable surface area (leading to at least tenfold increase), the process utilized were generally very time consuming and energy intensive (taking up to at least 20 h high-energy grinding). Furthermore, the iron contamination induced by the use of stainless steel balls during the grinding process could also cause significant deactivation in catalysis application [15] but this problem could be resolved by using relatively

Abbreviations: CHFS, continuous hydrothermal flow synthesis; A-sc-LCM, As-prepared mixture that was synthesized via CHFS route; A-cr-LCM, As-prepared mixture that was synthesized via citrate route; sc-LCM, LaCoO₃/MgO composite perovskite that was synthesized via CHFS route; cr-LCM, LaCoO₃/MgO composite perovskite that was synthesized via citrate route.

* Corresponding authors at: Department of Environmental Engineering, Zhejiang University, Hangzhou 310027, PR China. Tel.: +86 571 87953088; fax: +86 571 87953088.

E-mail addresses: xlweng@zju.edu.cn (X. Weng), zbwu@zju.edu.cn (Z. Wu).

more expensive tungsten carbide balls [16]. In comparison, forming composite perovskites could not only effectively hinder the perovskite particles sintering (via introducing sintering barrier, such as MgO [13] or Ce_xZr_{1-x}O₂ [5]) but also simultaneously enhance their catalytic activities (via interacting with the sintering barrier [14]). As such, there are two underlying themes existing in the desirable attributes for better composite perovskites: (1) high dispersion of perovskites over the sintering barrier to retain a high surface area after calcination; (2) the interaction between them to induce more labile oxygen and hence better catalytic activity.

Our previous work has demonstrated the advantage of a facile synthesis route (continuous hydrothermal flow synthesis route, referred as CHFS) in producing Pd/Ce_{1-x}Zr_xO₂/Al₂O₃ composite catalyst. The CHFS process effectively involves mixing a solution containing one or more metal salts, meeting with a stream of supercritical (or superheated) water, whereupon a simultaneous co-precipitation of very high surface area nano-sized crystallites occurs in a matter of seconds at ca. 450 °C and 24.1 MPa. The resultant products showed a high dispersion and strong interaction of Pd over Ce_{1-x}Zr_xO₂/Al₂O₃ support, which led to good performance in toluene oxidation [17] and three-way catalysis (TWC) application [18]. The unusual and rapid crystallising environment makes the CHFS route very effective for the syntheses of highly active composite catalysts. Hence, it could be a promising route to produce composite perovskites with higher surface area and better catalytic activity.

To verify this, the CHFS route was utilized herein for the synthesis of LaCoO₃/MgO composite perovskite (hereafter denoted as sc-LCM), where the LaCoO₃ was selected due to its reported easily forming surface anion vacancies [10] and the MgO is a well-known sintering barrier with high thermal stability [19]. Since the slight variation in catalytic reaction conditions, e.g. space velocity and/or reactant/oxygen molar ratio, could easily lead to significant difference in catalytic performance [20], it is very difficult to compare our catalyst with those reported in the literature due to the varied reaction conditions. As such, a compositional identical catalyst (hereafter denoted as cr-LCM) was synthesized in this paper via a well-known citrate route [21], which was then tested under an identical condition to that of sc-LCM catalyst for acceptable comparison. Furthermore, both of the samples were subjected to XRD, HAADF STEM, HR-TEM, BET, H₂-TPR, O₂-TPD analytical techniques to measure their textual and redox properties, where toluene and methane were selected as probes to access their catalytic performances in low- and high-temperature ranges, respectively.

2. Experimental details

2.1. Materials

[La(NO₃)₃·6H₂O, ≥99.0%], [Co(NO₃)₂·6H₂O, ≥99.0%], [Mg(NO₃)₂·6H₂O, ≥99.0%] and potassium hydroxide pellets (KOH, ≥96.0%) were supplied by Sinopharm Chemical Reagent Co. Ltd. (Shanghai, China). All chemicals were used as obtained. Deionized water was used in all experiments.

2.2. General syntheses

2.2.1. CHFS route

Briefly, for the synthesis of 1:2 molar ratio of LaCoO₃/MgO composite perovskite, a 500 mL aqueous mixture solution of La(NO₃)₃ (0.05 M), Co(NO₃)₂ (0.05 M) and Mg(NO₃)₂ (0.1 M) was pumped (via P2, see Supplementary Fig. S1) to meet a flow of NaOH solution (1 M, via P3) at room temperature and this mixture then met superheated water (pumped via P1) at a mixing point (a 3/8" counter-current mixer, as described elsewhere [22]), whereupon

rapid co-precipitation of crystalline products occurred. The aqueous suspension was cooled via a water jacket cooler, passed through a 7 μm in-line filter and the resultant suspension was collected from the exit of a back-pressure regulator. Solids were recovered by centrifuging the suspension and then freeze-dried to obtain products as black colored fluffy powder. The as-prepared product (hereafter denoted as A-sc-LCM) was subsequently heat-treated in static air at an optimized condition (700 °C for 2 h) to yield LaCoO₃/MgO composite perovskite (hereafter denoted as sc-LCM).

2.2.2. Citrate route

La(NO₃)₃ (0.05 M), Co(NO₃)₂ (0.05 M) and Mg(NO₃)₂ (0.1 M) and citric acid monohydrate (0.4 M) were used as starting materials. Aqueous solutions with molar ratio La:Co:Mg at 1:1:2 were prepared. The slurry was stirred and water was slowly evaporated at 80 °C in a rotary evaporator. The drying process was completed by heating the powder in a vacuum oven set at 110 °C overnight. The resultant powder was calcined at 400 °C for 3 h in static air to get rid of any organic compounds (hereafter denoted as A-cr-LCM) and then at 700 °C for 2 h in static air to yield LaCoO₃/MgO composite perovskite (hereafter denoted as cr-LCM).

2.3. Characterizations

Freeze-drying was performed using a Vacuum Freeze Dryer, Model LGJ-10C, supplied from Beijing Boyikang Laboratory Instruments Co. Ltd. the solids were first frozen for 4 h at -50 °C and then freeze-dried for 24 h at 10 Pa. XRD patterns were recorded by using a Rigaku D/Max RA diffractometer with Cu-Kα radiation ($\lambda = 0.15418 \text{ nm}$) at 40 kV and 150 mA and at an angle of 2θ from 20 to 70°. The dispersion of resultant products was investigated using a model Tecnai G² F20 S-TWIN (FEI Company, USA) high-resolution transmission electron microscope (HR-TEM, 400 kV accelerating voltage) instrument equipped with STEM, EDX and HAADF. BET surface areas (SBET) were determined using N₂ physisorption at 77 K, with a Micromeritics ASAP 2020 equipment. Sample degassing pre-treatment was conducted at 80 °C for 2 h under vacuum in order to remove adsorbed species. Thermogravimetric analyses (TGA) were carried out in air using a Polymer Labs simultaneous thermogravimetric analyser (STA 1500) at a heating rate of 10 °C min⁻¹. Gas Chromatography-Mass Spectrometry (GC-MS, Agilent 7890A GC & 5975C MSD) equipped with HP-5ms column were utilized to measure any organic compounds existing in the out-let gas from catalytic oxidation toluene tests. Gas Chromatography (GC, Agilent 7890A) equipped with GS-Gaspro and Poropak Q & 5 Å columns was utilized to measure CO₂ and CO existing in the out-let gas from catalytic oxidation either toluene or methane tests.

2.3.1. H₂-TPR

The details of H₂-TPR test were as follows. Step 1 (pre-treatment step) in which samples (0.05 g) were heated to 400 °C with a dwelling time of 1 h and then cooled down to room temperature. The process was operated with a purge of flowing O₂ gas at the rate of 30 mL min⁻¹; Step 2 (TPR step) in which samples were pre-treated at 100 °C for 40 min and then heated up from 100 to 800 °C under a purge of flowing H₂/N₂ (6% H₂ in N₂) at 35 mL min⁻¹.

2.3.2. O₂-TPD

Accurately measured 0.3 g sample was pre-treated at 500 °C for 2 h with a purge of flowing O₂ gas at the rate of 30 mL min⁻¹; After the temperature was slowly cooled down to room temperature, followed by a He purge with a flow rate of 50 mL min⁻¹ for 40 min, the sample was heat-treated from 40 to 800 °C to evaluate oxygen desorption.

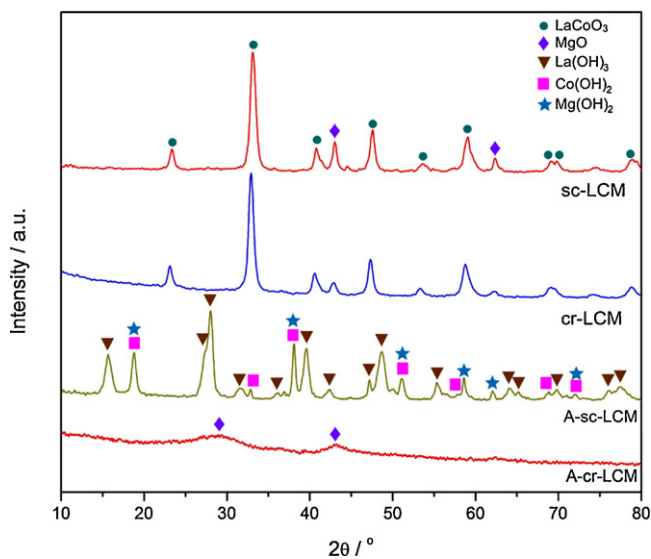


Fig. 1. X-ray powder diffraction patterns of LCM samples.

2.4. Catalytic oxidation test

2.4.1. Toluene oxidation test

The activities of samples were measured in a fixed bed reactor. The 6-mm i.d. quartz reactor tube was loaded with 0.50 g catalyst powder (mixed with quartz sand to yield the totally volume at 1 mL) and placed in an electrically heated furnace. The flow rate was set to maintain the gas hourly space velocity (GHSV) at 10,200 h⁻¹ for all the runs. A nitrogen stream (flow rate = 20 mL min⁻¹) was bubbled through a saturator filled with liquid toluene in a water bath at 40 °C, which was then mixed with 10% O₂/N₂ gas stream, to keep the inlet concentration of gaseous toluene at ca. 500 ppm, N₂: 135 mL min⁻¹, O₂: 10 mL min⁻¹ and N₂: 25 mL min⁻¹ (bubbling). Prior to the tests, all samples were pre-treated under a purge of the mixed gas at 110 °C until the stabilization of the system. The reactants and products were analyzed using GC-MS (Agilent Technologies 7890A GC & 5975C MSD) and/or GC analyzer (Agilent Technologies 7890A). No other carbon-containing organic compounds were detected at T_{90} (i.e. 90% conversion of toluene).

2.4.2. Methane oxidation test

The activities of samples were measured in a fixed bed reactor. The 10 mm i.d. steel tube was loaded with 0.50 g catalyst powder (mixed with quartz sand to yield the totally volume at 1 mL) and placed in an electrically heated furnace. The flow rate was set to maintain the gas hourly space velocity (GHSV) at 9600 h⁻¹ for all the runs. The reactant feed rate (total at 160 mL min⁻¹) was controlled by mass flow controllers containing 1% CH₄, 10% O₂ with balance N₂. Prior to the tests, all samples were pretreated at 400 °C for 1 h under a purge of balance N₂. The reactants and products were analyzed using GC analyzer (Agilent Technologies 7890A GC) equipped with a flame ionization detector (FID) and a thermal conduction detector (TCD). No CO was detected at T_{90} (i.e. 90% conversion of methane).

3. Results and discussion

3.1. X-ray powder diffraction

Phase identities and purities of samples were elucidated using X-ray powder diffraction (XRD). As shown in Fig. 1. For as-prepared samples, the A-sc-LCM sample revealed the characteristic peaks of La(OH)₃ (JCPDS 36-1481), Co(OH)₂ (JCPDS 45-0031) and Mg(OH)₂

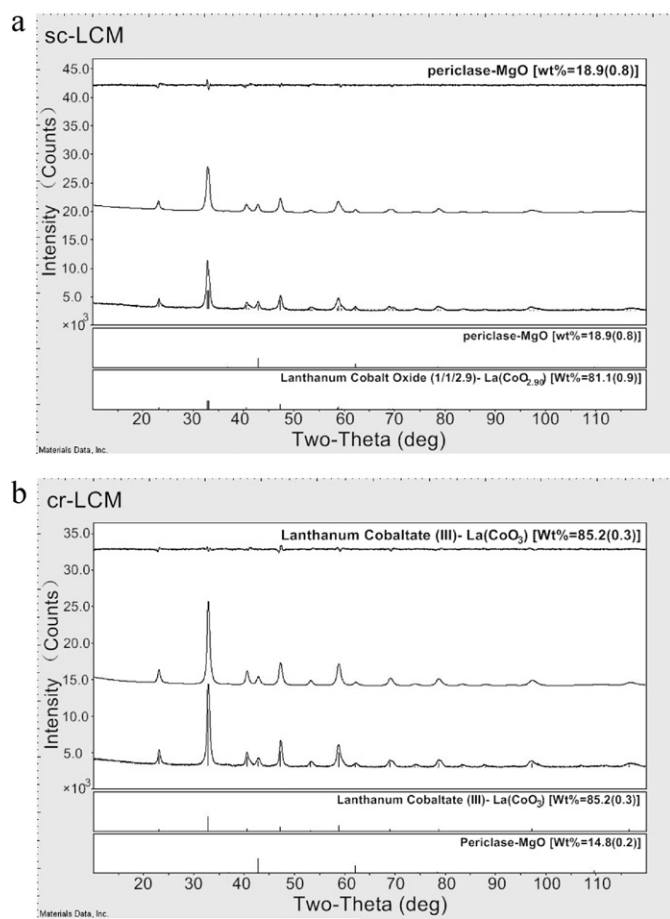


Fig. 2. Rietveld refinement patterns of LCM samples.

(JCPDS 44-1482) mixture whilst the A-cr-LCM sample show several weak peaks mainly attributing to MgO (JCPDS 30-0794), where little XRD peaks assigned to La and Co related species were observed, presumably due to their very low crystallinity. Further heat-treatment of the two as-prepared samples at 700 °C for 2 h in static air both yielded LaCoO₃/MgO composite perovskites (where the pattern for LaCoO₃ at JCPDS 48-0123 and for MgO at JCPDS 65-0467). The crystallite sizes of LaCoO₃ were estimated using XRD peak halfwidths (applying the Scherrer equation), which did not show obvious difference in the two samples (10.0 nm for sc-LCM and 10.9 nm for cr-LCM). However, for MgO crystallite, the sc-LCM sample revealed the size at 15.9 nm, larger than those in the cr-LCM sample (at 12.4 nm).

Rietveld refinement analyses (see Fig. 2) were performed over the sc-LCM and cr-LCM samples to evaluate their structural configurations. The LaCoO₃ phase in the sc-LCM sample had a rhombohedral symmetry of space group ($R\bar{3}c$) with $a=b=0.544$ nm and $c=1.316$ nm, which is similar to a LaCoO_{2.9} perovskite [23] ($a=b=0.544$ nm and $c=1.303$ nm) but with larger c value. We proposed that the prolongation in the c axis of sc-LCM sample could be attributed to the partial insertion of Mg²⁺ (ionic radius = 0.065 nm) into its B site (Co³⁺, ionic radius = 0.063 nm) forming LaMg_xCo_{1-x}O_{3-d} perovskite because a similar phenomenon was also observed by Toniolo et al. in their LaCo_xCu_{1-x}O_{3-d} perovskite [24]. In comparison, the LaCoO₃ phase in the cr-LCM sample had a cubic symmetry of space group ($Pm-3m$) with $a=b=c=0.384$ nm, showing the feature of an ideal perovskite structure [25]. Zhang et al. had indicated that the rhombohedral symmetry might lead to the most significant oxygen non-stoichiometry (i.e. forming oxygen vacancies) due to a

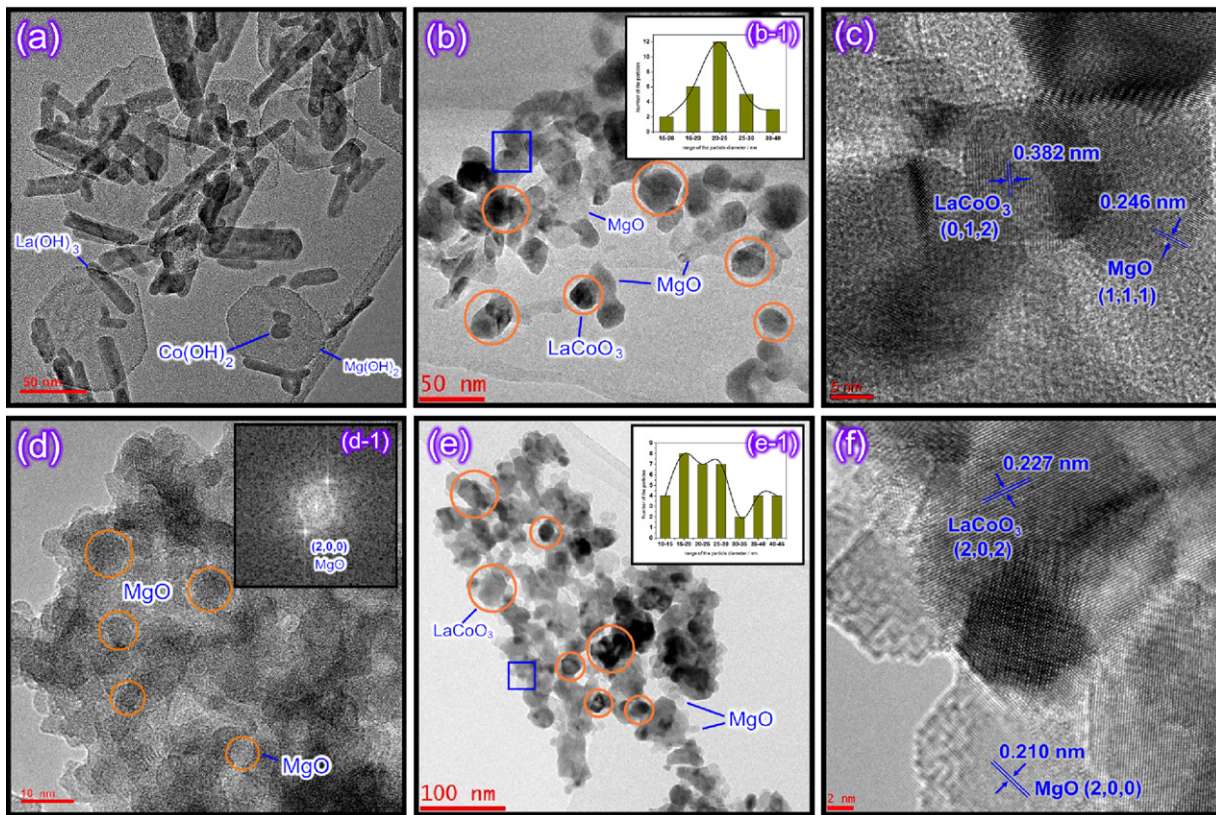


Fig. 3. HR-TEM images of (a) A-sc-LCM sample, (b) sc-LCM sample, (d) A-cr-LCM sample and (e) cr-LCM sample; (b-1) and (e-1) represent the corresponding particle size distribution; (d-1) shows a fast Fourier transform pattern of MgO in the A-cr-LCM sample; (c) and (f) show the d-spacing of LaCoO_3 and MgO in the sc-LCM and cr-LCM samples, respectively.

much more severe distortion in the crystal structure [10]. Since Fino et al. [26] had suggested that the catalytic oxidation over perovskites generally underwent a suprafacial process in low-temperature range (generally less than 400°C [27]), where weakly chemisorbed oxygen upon oxygen vacancies played a crucial role for the activity, the sc-LCM sample is expected possessing a better low-temperature catalytic activity than the cr-LCM sample due to its possible presence of higher oxygen deficiency that was compensated by abundant oxygen vacancies as well as weakly chemisorbed oxygen. This would be verified in the following characterizations.

3.2. High-angle annular dark-field scanning transmission electron microscopy (HAADF-STEM)

To evaluate the dispersion of the as-prepared samples, the samples were then subjected to HAADF-STEM analyses. As expected, the A-sc-LCM sample revealed a good dispersion of its respective hydroxides (see Supplementary Fig. S2a), where EDX mapping La, Co, Mg elements all showed relatively similar patterns at a ca. $500\text{ nm} \times 500\text{ nm}$ scanning region, which is consistent with our previous reports [17,18,28]. In comparison, the A-cr-LCM sample showed relatively more aggregated EDX mapping patterns (see Supplementary Fig. S2b) at a same scanning region to that of A-sc-LCM sample but also revealed a good dispersion for its respective oxides/hydroxides.

After subjected to HR-TEM analyses, the A-sc-LCM sample (see Fig. 3a) revealed that highly crystalline hexagon-like $\text{Co}(\text{OH})_2$ plate (ca. 40 nm in diameter) and $\text{La}(\text{OH})_3$ needles (ca. $40\text{ nm} \times 10\text{ nm}$) were well dispersed on much larger $\text{Mg}(\text{OH})_2$ (ca. $80\text{ nm} \times 100\text{ nm}$) supports whilst the A-cr-LCM sample showed relatively aggregated morphology and only MgO particles were detected at the particle

size of ca. 5 nm (see Fig. 3d), where the La or Co related compounds were hardly to be clearly distinguished. After heat-treatment (see Fig. 3b and c), the sc-LCM sample revealed highly crystalline LaCoO_3 particles with major size at ca. 20 nm being well dispersed onto irregular-shape MgO particles (mean size at ca. $40\text{ nm} \times 40\text{ nm}$), whilst the cr-LCM sample (see Fig. 3e and f) showed an aggregated morphology with the particle size in a range of $10\text{--}45\text{ nm}$. Since the LaCoO_3 and MgO particles in the cr-LCM sample revealed similar particle size distribution, it is quite difficult to distinguish them clearly in its TEM image. In addition, the respective oxides were all confirmed via EDX analyses (see Supplementary Fig. S3).

BET surface area measurements were in good consistency with the HR-TEM results, which revealed that the cr-LCM sample had a surface area of $17.3\text{ m}^2\text{ g}^{-1}$, similar to the $\text{LaMnO}_3/\text{MgO}$ ($18\text{--}20\text{ m}^2\text{ g}^{-1}$) composite perovskites reported in the literature [12]. However, it was two-fold lower than that of sc-LCM sample (at $35.3\text{ m}^2\text{ g}^{-1}$). In particular, it should be also noted that since the TEM observation has shown that in the sc-LCM sample, the MgO particles were much larger than LaCoO_3 perovskites, the BET surface area exposed per unit perovskites of the sample should be higher than $35.3\text{ m}^2\text{ g}^{-1}$. This result is promising as it verifies our previous assumption that the CHFS could be a promising route for the syntheses of composite perovskites with higher surface area.

In literature, the utilization of sintering barrier was originated from the design of three-way catalysts (TWCs) [29], where $\gamma\text{-Al}_2\text{O}_3$ was employed as sintering barrier to inhibit the sintering of $\text{Ce}_x\text{Zr}_{1-x}\text{O}_2$ (CZ) particles due to the severe operating temperature of TWCs (can reach $>1000^\circ\text{C}$ in a close-coupled converter [30,31]). The originally designed sintering inhibition was mainly based on an “among dispersion” model (see Fig. 4a), where highly dispersed $\gamma\text{-Al}_2\text{O}_3$ particles could effectively avoid the inter-contacting of CZ

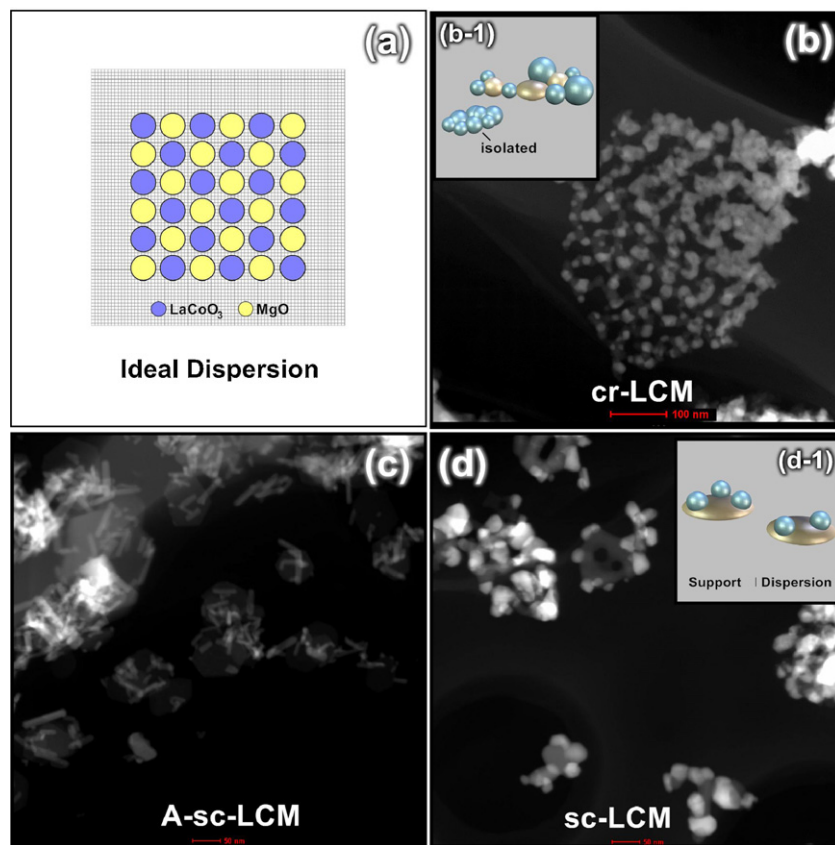


Fig. 4. (a) An ideal dispersion model as reported in the literature; (b) HAADF image of cr-LCM sample; (c) HAADF image of A-sc-LCM sample; (d) HAADF image of sc-LCM sample; (b-1) represents a resulted “among dispersion” model by non-ideal dispersion; (d-1) represent a “support dispersion” model.

particles, hence inhibiting their sintering. Although this model had resulted in significant outcome in terms of the high thermal stability of resultant CZ particles, it required an ideal dispersion of γ -Al₂O₃ among the CZ particles, otherwise the isolated CZ particles would still be sintered during ageing, leading to non-uniform particle size distribution of the CZ particles (see the case in the cr-LCM sample of Fig. 4b). As such, the “among dispersion” model might not be very propitious to the LCM composite perovskites, which required not only sintering inhibition but also more perovskites interacting with the support (i.e. MgO in the case) to yield abundant labile oxygen for better catalytic activity. The presence of isolated perovskites (due to non-ideal dispersion in the “among dispersion” model) could to some extent limit the contacting of LaCoO₃ perovskites with MgO, reducing their labile oxygen and hence lowering the catalytic performance.

From the HR-TEM results, we can see that the A-sc-LCM sample revealed a different model of “support dispersion” from that of A-cr-LCM sample, where the Co(OH)₂ and La(OH)₃ particles were mainly present on Mg(OH)₂ support (see Fig. 4c). This could be caused due to the significantly different particle sizes of Co(OH)₂, La(OH)₃ and Mg(OH)₂, where during the CHFS process, these simultaneously co-precipitated metal hydroxides would immediately inter-disperse due to the gas-like diffusivity of supercritical water [32], transferring the smaller metal hydroxides (e.g. Co(OH)₂ and La(OH)₃) onto larger ones (e.g. Mg(OH)₂). We proposed that this “support dispersion” model could not only ensure the functioning of MgO as sintering barriers (leading to a higher surface area at ca. 35.3 m² g⁻¹) but also induce more LaCoO₃ particles contacting with the MgO support (as the majority of them were present on the MgO surface, see Fig. 4d), resulting in the insertion of Mg²⁺ into the structure and yielding significant oxygen vacancies as well as weakly chemisorbed oxygen.

3.3. H₂-TPR and O₂-TPD analyses

To verify this, H₂-TPR and O₂-TPD were performed within a temperature range of 100–800 °C over the LCM samples. H₂-TPR plot (see Fig. 5a) of sc-LCM sample showed three hydrogen consumption peaks centered at ca. 245, 323, 370 °C, where the first reduction peak was presumably assigning to the reduction of oxygen ad-species [10] and the latter two peaks were due to the reduction of Co³⁺ to Co²⁺ [24]. The peak centered at 650 °C was attributed to the reduction of Co²⁺ to Co⁰ [10]. Comparing to unsupported LaCoO₃ perovskite that was also synthesized via the CHFS route, a low-temperature shifting could be observed in the sc-LCM sample. This improved reducibility has been attributed to Mg²⁺ partial substitution into the perovskite structure by Cimino et al. [14] in their LaMnO₃/MgO composite perovskite, which was consistent with our aforementioned Rietveld refinement results. For cr-LCM sample, the reduction peak of oxygen ad-species was absent, which is unsurprising given the lack of oxygen vacancies due to the presence of ideal perovskite structure. Its reduction peaks (centered at ca. 358, 401, 674 °C, respectively) had all shown a higher temperature shifting comparing to those of sc-LCM sample, indicating a lower reducibility for the sample.

O₂-TPD plot generally showed three oxygen desorption regions as indicated in Fig. 5b, where the lower temperature region (denoted as α -O) corresponded to weakly chemisorbed oxygen upon oxygen vacancies, the intermediate region (denoted as α' -O) was ascribed to near-surface oxygen that is absorbed to lattice defects and the higher temperature region (denoted as β -O) was assigned to lattice oxygen [33]. It can be seen that the sc-LCM sample had a much lower α -O desorption than the cr-LCM sample, which was in good agreement with the H₂-TPR analyses. Furthermore, the amounts of near-surface oxygen α' -O and lattice oxygen

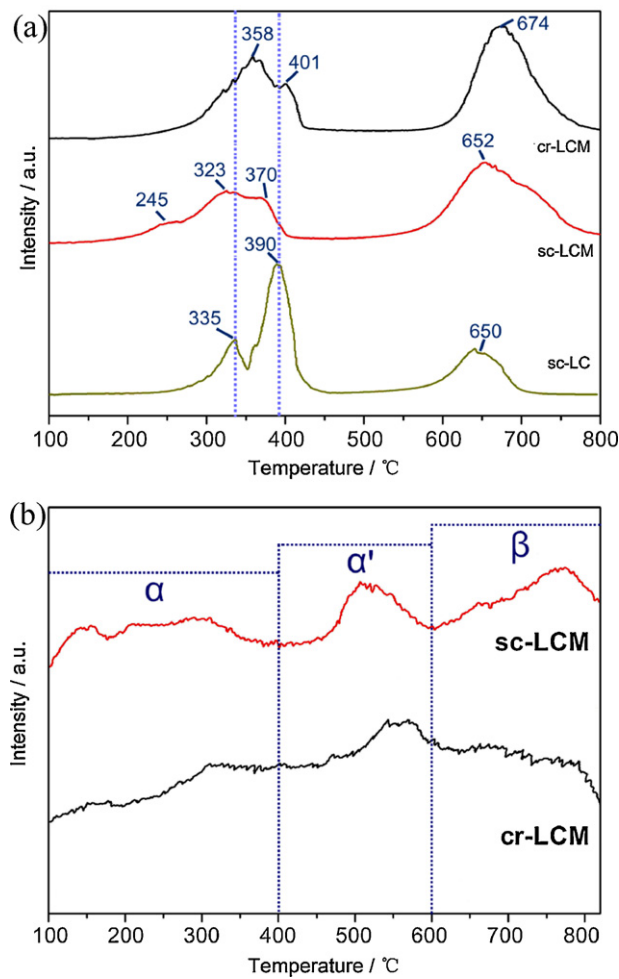


Fig. 5. (a) H₂-TPR and (b) O₂-TPD profiles for LCM samples.

β -O in the sc-LCM sample were also significantly higher than those of cr-LCM sample. This could be due to that the sc-LCM sample had a more distorted symmetry (*R*-3c) than the cr-LCM sample (*Pm*-3*m*), which led to the presence of more lattice defects in perovskite structure and hence easy desorption of α' -O and β -O oxygen.

In literature, Rossetti and Forni [27] had indicated that the catalytic oxidation over perovskites generally follows two possible mechanisms, suprafacial and intrafacial ones. The former dominated the catalytic process at lower temperature range ($T < 400$ °C), where the weakly chemisorbed oxygen, i.e. α -O, plays a crucial role in the activity, whilst the latter is active at $T > 400$ °C and strongly related with the mobility of near-surface oxygen α' -O and lattice oxygen β -O, both of which are continuously replaced by gaseous oxygen through a Mars–Van Krevelen mechanism. As such, according to the BET, H₂-TPR and O₂-TPD results, we could foresee that the sc-LCM sample that possessed higher BET surface area and better oxygen reduction and desorption capability would yield a better catalytic activity than the cr-LCM sample in either low- or high-temperature ranges.

3.4. Catalytic activity tests

To verify this, toluene, a typical VOC that has been extensively utilized in making paints, paint, thinners, lacquers, adhesives and rubber [34], was selected as an probe to access the activity at low-temperature range, whereas methane, a natural gas utilized in fuelled burners for gas turbine power generation [14], whose

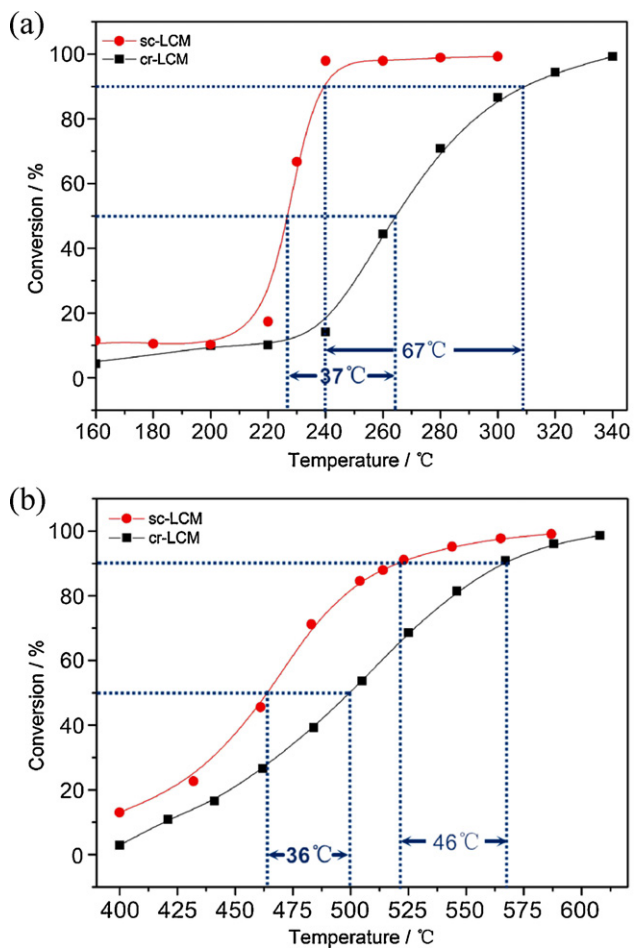


Fig. 6. (a) Toluene conversion as a function of temperature for LCM samples. Gas hourly space velocity (GHSV) at 10,200 h⁻¹, toluene at ca. 500 ppm, N₂: 135 mL min⁻¹, O₂: 10 mL min⁻¹; (b) methane conversion as a function of temperature for LCM samples. Gas hourly space velocity (GHSV) at 9600 h⁻¹, methane at ca. 10,000 ppm, N₂: 142 mL min⁻¹, O₂: 16 mL min⁻¹.

total oxidation temperature generally above 400 °C [12–14,27,35], was chosen as an probe to access the high-temperature activity.

In toluene oxidation tests, both of the samples were subjected to a feed steam containing ca. 500 ppm toluene with a gas hourly space velocity (GHSV) at 10,200 h⁻¹. As shown in Fig. 6a, the cr-LCM sample revealed a light-off temperature (T_{50} , 50% conversion of toluene) at ca. 262 °C, which rose progressively with temperatures and achieved completed conversion when temperature was up to 307 °C (total oxidation temperature, T_{90} , i.e. 90% conversion of toluene). The performance of cr-LCM sample was relatively similar to that reported by Rousseau et al. [36] although this comparison might not be very convinced as their reaction conditions were different (its inlet concentration of toluene was at 500 ppm but with a much lower GHSV at 5700 h⁻¹). Nevertheless, the cr-LCM sample showed a relatively lower light-off temperature (T_{50}) at ca. 226 °C but with a remarkable T_{90} at only ca. 240 °C, revealing a significantly higher activity than the cr-LCM sample, which was in consistence with the aforementioned analyses.

In methane oxidation tests, both of the samples were subjected to a feed steam containing ca. 10,000 ppm methane with a gas hourly space velocity (GHSV) at 9600 h⁻¹. As shown in Fig. 6b, the cr-LCM sample showed a light-off temperature (T_{50}) at ca. 500 °C, which was relatively higher than that of sc-LCM sample ($T_{50} = 464$ °C). The T_{90} of cr-LCM sample was measured at ca. 567 °C, showing a comparatively lower activity than that of sc-LCM sample ($T_{90} = \text{ca. } 521$ °C), also in good agreement with the aforementioned

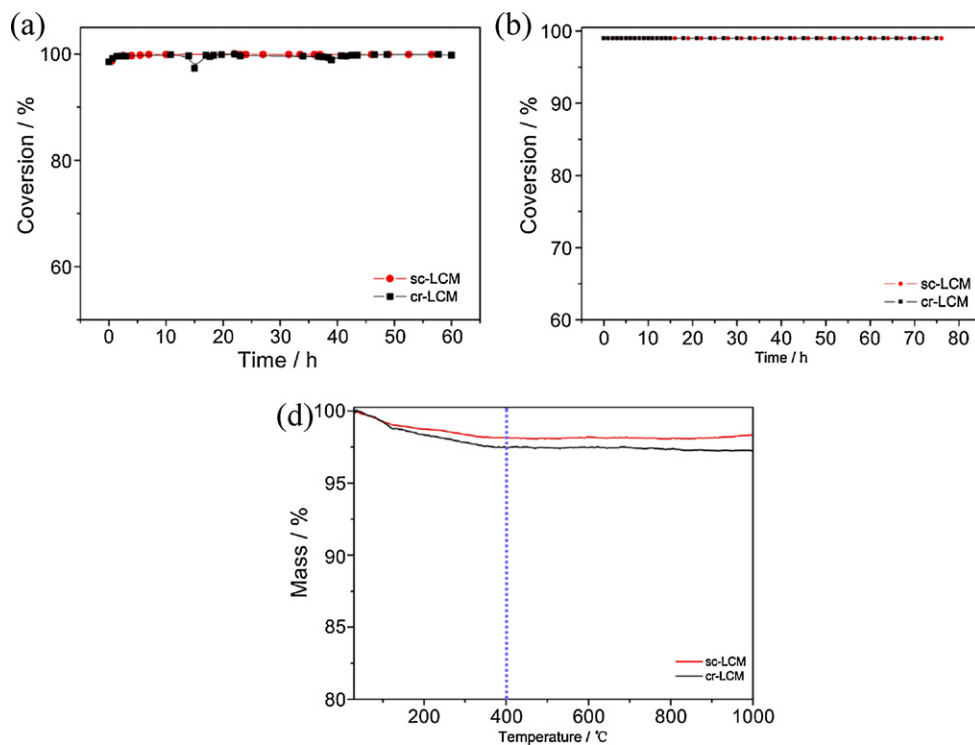


Fig. 7. Durability tests for (a) toluene oxidation and (b) methane oxidation over LCM samples; (c) TGA plots for LCM samples.

analyses. To the best of our knowledge, there were few reports in literature for LCM samples utilized in methane oxidation. Saracco et al. had reported the $\text{LaMnO}_3/\text{MgO}$ [12] and $\text{LaCrO}_3/\text{MgO}$ [13] catalysts in the application of methane oxidation, which both showed comparatively lower activity than our sc-LCM sample. However, due to the varied conditions in GHSV and inlet concentration of methane, this comparison was still argued. Furthermore, through GC-MS or GC analyses on the out-let gases from either toluene or methane oxidation tests (see Supplementary Figs. S4 and S5), both of sc-LCM and cr-LCM samples showed a full conversion of respective reactants to CO_2 and H_2O at T_{90} during the tests, where no other organic compounds and CO were detected in toluene and methane oxidation tests, respectively.

Since one may also concern the stability of the composite perovskites, a durability test over the cr-LCM and sc-LCM samples were also conducted in this paper. Fig. 7a shows the resultant toluene oxidation durability tests for cr-LCM (at $T_{100} = 300^\circ\text{C}$) and sc-LCM (at $T_{100} = 340^\circ\text{C}$) samples, both of which did not show obvious deactivation, revealing a good stability for the samples. Similarly, under the methane oxidation durability tests at $T_{100} = 600^\circ\text{C}$ (see Fig. 7b), both of the samples also show good stability. Since it is well-known that the catalysts under methane oxidation tests could easily undergo a deactivation process due to the formation of carbon filaments or coke on the surface, the after-tested samples were then subjected to thermogravimetric analyses (TGA). As shown in Fig. 7c, there were no obvious weight losses observed for both samples at the temperature $\geq 400^\circ\text{C}$ (where this temperature range was reported to be associated to the decomposition of coke and/or carbon filaments present on the catalyst surface [24]), revealing a good resistance to coke and/or carbon filaments for the LCM samples.

Based on the aforementioned analyses, we can conclude that the sc-LCM sample had a higher activity than the cr-LCM sample in both low- and high-temperature ranges. The “support dispersion” feature of sc-LCM sample had resulted in higher BET surface area and better oxygen adsorption and desorption capability comparing to the cr-LCM sample (with “among dispersion feature”), which

were accounted for its good catalytic performance in toluene and methane oxidation tests. The result reported herein is promising and further prove the significant advantage of CHFS route, which is able to produce highly active composite perovskites, owing to its capability in yielding highly dispersed and rather interacted perovskite/sintering barrier. In addition, it should be also noted that although the sc-LCM sample had shown good catalytic performance, its catalytic activity can be further improved via partial substitution of A and/or B sites in perovskite structure [10]. This approach is currently pursuing, the results of which will be reported in due course.

4. Conclusions

We have explored a relatively green and facile CHFS route for the syntheses of highly active $\text{LaCoO}_3/\text{MgO}$ composite perovskite. Although the citrate route had also resulted in a good dispersion for its products, the presence of “among dispersion” feature led to the lower BET surface area and oxygen adsorption and desorption than the sc-LCM sample (with “support dispersion” feature). The unusual and rapid crystallizing environment of the CHFS route was shown able to produce highly dispersed and rather interacted composite perovskite, which were accounted for its good performance in toluene and methane oxidations. We expect that the work conducted herein could generate more awareness onto the origin of this novel CHFS technique and give a new thought for the design of composite perovskites with higher surface area and better catalytic activity.

Acknowledgements

The project was financially supported by Changjiang Scholar Incentive Programme (2009), Ministry of Education, PR China, the Fundamental Research Funds for the Central Universities

(2012QNA6005) and Zhejiang Provincial Natural Science Foundation of China (LQ12E08011).

Appendix A. Supplementary data

Supplementary data associated with this article can be found, in the online version, at <http://dx.doi.org/10.1016/j.apcatb.2012.07.020>.

References

- [1] S. Lambert, C. Cellier, P. Grange, J.P. Pirard, B. Heinrichs, *Journal of Catalysis* 221 (2004) 335–346.
- [2] K. Okumura, T. Kobayashi, H. Tanaka, M. Niwa, *Applied Catalysis B – Environmental* 44 (2003) 325–331.
- [3] C.H. Kim, G.S. Qi, K. Dahlberg, W. Li, *Science* 327 (2010) 1624–1627.
- [4] D.A. Slade, A.M. Duncan, K.J. Nordheden, S.M. Stagg-Williams, *Green Chemistry* 9 (2007) 577–581.
- [5] M. Alifanti, M. Florea, V.I. Parvulescu, *Applied Catalysis B – Environmental* 70 (2007) 400–405.
- [6] J.M. Giraudon, A. Elhachimi, F. Wyrwalski, S. Siffert, A. Aboukais, J.F. Lamonier, G. Leclercq, *Applied Catalysis B – Environmental* 75 (2007) 157–166.
- [7] H.F. Huang, Z. Sun, H.F. Lu, L.Q. Shen, Y.F. Chen, *Reaction Kinetics and Catalysis Letters* 101 (2010) 417–427.
- [8] M. Zawadzki, J. Trawczynski, *Catalysis Today* 176 (2011) 449–452.
- [9] J.M. Wu, W. Wen, *Environmental Science and Technology* 44 (2010) 9123–9127.
- [10] R.D. Zhang, N. Luo, B.H. Chen, S. Kaliaguine, *Energy and Fuels* 24 (2010) 3719–3726.
- [11] R.D. Zhang, A. Villanueva, H.S. Alamdari, S. Kaliaguine, *Applied Catalysis B – Environmental* 64 (2006) 220–233.
- [12] G. Saracco, F. Geobaldo, G. Baldi, *Applied Catalysis B – Environmental* 20 (1999) 277–288.
- [13] G. Saracco, G. Scibilia, A. Iannibello, G. Baldi, *Applied Catalysis B – Environmental* 8 (1996) 229–244.
- [14] S. Cimino, L. Lisi, R. Pirone, G. Russo, M. Turco, *Catalysis Today* 59 (2000) 19–31.
- [15] S. Royer, F. Berube, S. Kaliaguine, *Applied Catalysis A – General* 282 (2005) 273–284.
- [16] M. Ghasdi, H. Alamdari, S. Royer, A. Adnot, *Sensors and Actuators B – Chemical* 156 (2011) 147–155.
- [17] X.L. Weng, J.Y. Zhang, Z.B. Wu, Y. Liu, H.Q. Wang, J.A. Darr, *Green Chemistry* 13 (2011) 850–853.
- [18] X.L. Weng, J. Zhang, Z. Wu, Y. Liu, H. Wang, J.A. Darr, *Applied Catalysis B – Environmental* 103 (2011) 453–461.
- [19] M. Berg, S. Jaras, *Catalysis Today* 26 (1995) 223–229.
- [20] J.G. Deng, H.X. Dai, H.Y. Jiang, L.Zhang, G.Z. Wang, H. He, C.T. Au, *Environmental Science and Technology* 44 (2010) 2618–2623.
- [21] J.G. Deng, L.Zhang, H.X. Dai, H. He, C.T. Au, *Industrial and Engineering Chemistry Research* 47 (2008) 8175–8183.
- [22] E. Lester, P. Blood, J. Denyer, D. Giddings, B. Azzopardi, M. Poliakoff, *Journal of Supercritical Fluids* 37 (2006) 209–214.
- [23] P.G. Radaelli, S.W. Cheong, *Physical Review B* 66 (1–9) (2002), 094408.
- [24] F.S. Toniolo, R.N.S.H. Magalhaes, C.A.C. Perez, M. Schmal, *Applied Catalysis B – Environmental* 117 (2012) 156–166.
- [25] M.A. Pena, J.L.G. Fierro, *Chemical Reviews* 101 (2001) 1981–2017.
- [26] D. Fino, N. Russo, G. Saracco, V. Speechia, *Journal of Catalysis* 217 (2003) 367–375.
- [27] I. Rossetti, L. Forni, *Applied Catalysis B – Environmental* 33 (2001) 345–352.
- [28] X.L. Weng, J. Zhang, Z. Wu, Y. Liu, *Catalysis Today* 175 (2011) 386–392.
- [29] A. Morikawa, T. Suzuki, T. Kanazawa, K. Kikuta, A. Suda, H. Shinjo, *Applied Catalysis B – Environmental* 78 (2008) 210–221.
- [30] J. Kaspar, R. Di Monte, P. Fornasiero, M. Graziani, H. Bradshaw, C. Norman, *Topics in Catalysis* 16 (2001) 83–87.
- [31] M. Ozawa, *Journal of Alloys and Compounds* 275–277 (1998) 886–890.
- [32] A. Kruse, E. Dinjus, *Journal of Supercritical Fluids* 39 (2007) 362–380.
- [33] R. Pereniguez, J.L. Hueso, J.P. Holgado, F. Gaillard, A. Caballero, *Catalysis Letters* 131 (2009) 164–169.
- [34] K.J. Kim, H.G. Ahn, *Applied Catalysis B – Environmental* 91 (2009) 308–318.
- [35] A.K. Datye, J. Bravo, T.R. Nelson, P. Atanasova, M. Lyubovsky, L. Pfefferle, *Applied Catalysis A – General* 198 (2000) 179–196.
- [36] S. Rousseau, S. Loridant, P. Delichere, A. Boreave, J.P. Deloume, P. Vernoux, *Applied Catalysis B – Environmental* 88 (2009) 438–447.